A Mechanism for the Southward Propagation of Mesoscale Convective Systems Over the Bay of Bengal

Deepeshkumar Jain[1] *, Arindam Chakraborty[1,2], Ravi S. Nanjundiah[1,2,3]

Deepeshkumar Jain, deepesh@caos.iisc.ernet.in

[1]Centre For Atmospheric and Oceanic Sciences, Indian Institute of Science, Bangalore, India

[2]Divecha Centre for Climate Change, Indian Institute of Science, Bangalore, India

[3]Indian Institute of Tropical Meteorology, Pune, India

*Centre For Atmospheric and Oceanic Sciences, Indian Institute of Science

This article has been accepted for publication and undergone full peer review but has not been through the copyediting, typesetting, pagination and proofreading process, which may lead to differences between this version and the Version of Record. Please cite this article as doi: 10.1002/2017JD027470

Abstract. Equator-ward propagating precipitation episodes over the Bay of Bengal have been documented in many previous observational studies. Proposed propagation mechanisms include mean surface to mid-tropospheric wind shear driving the convection orthogonal to the lower tropospheric winds and the gravity currents generated by outflow from convection initiated by the diurnally-varying land-ocean circulations dispersing south. In this study, we perform high resolution simulations using the Weather Research and Forecast model capable of resolving mesoscale convective systems during the South Asian summer monsoon season. This mesoscale system is shown to have squall-line like structure with leading line/trailing stratiform. The rear inflow, due to saturated downdraft, and jump updraft indicates a gravity current-like structure. The rear inflow jet produces horizontal momentum tendencies in the direction of propagation. The center of convection is shown to move faster than the mid-tropospheric winds and at the same speed as that of the rear inflow jet near the surface. These systems are also shown to be tightly coupled to the diurnal land surface heating cycle. We perform additional model simulations with varying horizontal resolution and with the inclusion of cumulus parameterization. Model with cumulus parameterization is unable to simulate the updraft-downdraft pair and the gravity current structure of this southward propagating mesoscale system. We find that high model resolution is needed to resolve the updraft-downdraft pair and cumulus parameterization assumptions break down at such high resolutions. Using cloud mi-

crophysics exclusively becomes essential in simulating these mesoscale systems.

Keypoints:

- Mesoscale systems move south within northward moving synoptic scale cloud clusters.
- These systems have gravity current structure and propagate orthogonal to lower tropospheric winds.
- High resolution and cloud microphysics schemes are necessary to simulate these events using numerical models.

1. Introduction

The South Asian monsoon (monsoon hereafter) accounts for more than 75% of the total annual precipitation over the Indian region [Guhathakurta et al, 2015]. Since a large percentage of the 1.3 billion people of India depend on monsoon precipitation for their agricultural water supply [Gadgil and Gadgil, 2006], the importance of correct monsoon prediction can not be over emphasized. The monsoon is a remarkably regular annual phenomenon characterized by seasonal reversal in the direction of the wind [Gadgil, 2003]. It does however show a considerable variability in time and space [Gadgil, 2003]. The Bay of Bengal (BoB) is the location of some of the highest mean precipitation during monsoon, and the latent heating over BoB helps drive the monsoon circulation [Wang and Fan, 1999; Chakraborty et al, 2009]. Among the fundamental components of monsoon are the mesoscale convective systems (MCSs) which contribute to a large portion of monsoon precipitation [Wang, 2006]. MCSs are round or linear thunderstorm regions and include (among others) squall lines and Mesoscale Convective Complexes. The basic characteristics and features of MCSs have been discussed in Houze [2004]. Observational studies have reported equatorward propagating precipitation episodes over the BoB [Zuidema, 2003; Webster et al, 2002; Miyakawa and Satomura, 2006; Liu et al, 2008; Sahany et al, 2010]. These studies suggest that this signature may predominantly be caused by MCSs.

These diurnally generated MCSs have been shown to propagate southwards over the BoB and influence the diurnal cycle over the ocean [Sahany et al, 2010]. These MCSs are most prominent during the onset phase of the monsoon [Miyakawa and Satomura, 2006]. Zuidema [2003] showed that these southward moving cloud bands were consistent

with observed climatology using the data from Joint Air-Sea Monsoon Interaction Experiment research cruise (JASMINE, Webster et al [2002]). These MCSs had a southward component of propagation over the entire BoB even when the large scale movement of precipitation [Chakraborty and Nanjundiah, 2012], in association with convergence zone, was northwards. These large scale northward propagations show oscillations at intraseasonal time scales [Chattopadhyay et al, 2009; Choudhury and Krishnan, 2011]. The southward propagating MCSs embedded within these large scale northward propagations resemble the westward propagating clusters in the eastward propagating superclusters over the equator [Nakazawa, 1988]. Zuidema [2003] also examined the 3-hourly brightness temperature derived from the satellite infrared data to characterize the organizational features of the convection over the BoB. She found that the initiation of these convective systems was at the land-water interface north of BoB due to the diurnal heating of the land.

Houze [2004] attributed these MCSs to the diurnally generated gravity waves during the onset of the monsoon. Time-Latitude section (Fig 34 in Houze [2004] reproduced from Webster et al. (2002)) of the cloud brightness temperature showed high cloud tops propagating southward. He suggested that this south-southeastward direction of propagation could not be explained by mean advection and that the diurnally generated gravity waves over the coastal region south of Himalayas phase-locked with the convection offshore. The eventual MCS became one with the wave and propagated southward. Based on the radar images, these cloud systems were believed to be MCSs with squall-line like structure. Webster et al. (2002) showed that the radar images documented in JASMINE by C-band Doppler radar reveal the leading line/trailing stratiform like structure of these

systems. Consecutive radar images verified that these systems progressed southward with the leading convective line.

Miyakawa and Satomura [2006] found that the number of systems varied with time for the duration of analysis (April-October) with nearly a quarter of the total systems propagating equatorward. They concluded that the existence of a trough over the BoB at the height of 600 hPa was a favorable condition for the travel. They also found that the surface to 600 hPa wind shear had a southward component and attributed this to be the advective component of the southward propagating MCSs over the BoB. However, they also found that some systems moved much faster than mean velocity at any level and that the discrepancy may be attributed to rebuilding of convective cells provoked by cold pool outflows.

Liu et al [2008] emphasized that the life-time of traveling rainfall episodes was much longer compared to the individual convective system, suggesting that new deep convection was continually initiated as the system propagated. According to their study, these systems mostly initiated at about midnight over the ocean and during the day over coastal land. Based on their finding of the absence of a steering level by mean advection compared to other systems over the tropics, they stressed the importance of coupling between gravity waves and the convection over the BoB and that the system over the BoB resembled Kelvin waves and Madden-Julian oscillation in regard to convectively coupled wave. Their finding emphasized the significance of MCSs cold pool in determining the velocity of propagation in addition to the advective component reported by Miyakawa and Satomura [2006].

Monsoon and associated mesoscale structures are being studied using various observational data and reanalysis products [Virts and Houze Jr, 2016; Romatschke and Houze Jr, 2011; Liu et al, 2008]. However, season long simulations of the mesoscale structures have been limited due to the computational cost involved in simulating these systems at the desired resolution. Recent advancements in computing empower us to perform a season long high resolution model simulation capable of resolving mesoscale structures and investigate the underlying mechanisms. Many of the mesoscale structures during the monsoon have been missing from conventional coarse resolution general circulation model simulations and the reanalysis data sets. There have been no modelling studies of this southward propagating MCS. We analyzed few reanalysis datasets and coarse resolution general circulation model simulations and found this signal missing. In an attempt to simulate this MCS, we performed a season long (June-August) Weather Research and Forecast (WRF) model simulation at 3 km horizontal grid resolution with explicit microphysics scheme, i.e. cloud resolving model (CRM) resolution. The choice of the model was motivated by Medina et al [2010], who investigated the initiation of deep convection over the western and eastern Himalayan foothills using WRF in a three domain configuration, with their innermost domain having a horizontal resolution of 3 km. Their study showed the capability of WRF in capturing the dynamics involved with the initiation, intensification, orographic lift, and the role of BoB in controlling deep convection. Kataoka and Satomura [2005] showed the capability of non-hydrostatic cloud resolving model in simulating the correct diurnal cycle over Meghalayan plateau and initiation of MCSs which propagated south. They also emphasized the role of convective cold pool and gravity current-like structure in determining the speed of propagation of these MCSs.

Using our simulations, we investigated the dynamical and thermodynamical structure of this convective system. Since these MCSs have a major contribution to the overall precipitation over the region, it is important to understand the reasons behind failure of conventional general circulation models in simulating these systems irrespective of the model resolution. To that end, we carried out additional simulations for the month of June with horizontal resolutions of 3, 12, and 30 km while keeping the rest of the physics schemes the same. Additionally, we carried out these simulations while changing the convection representation from explicit microphysics to cumulus parameterization. In an additional CRM simulation with explicit microphysics we kept the land surface temperature constant for the month of June while sea surface temperature was allowed to evolve. This simulation was used to study the effects of diurnal land heating cycle on the initiation and propagation of these MCSs.

Section 2 discusses the model details and experimental setup used for the present study. Section 3 describes the data used to validate this study. Section 4 discusses results from the model, delves into the simulated structure of the MCSs and the effect of model resolution and convection scheme in the model. We then show the simulations having constant land surface temperature in June. We summarize the results in Section 5.

2. Model and Simulation Details

We use WRF version 3.4 for the present study. WRF is the Non-hydrostatic mesoscale model developed by Mesoscale and Microscale Meteorology Division of National Center for Atmospheric Research [Skamarock and Klemp, 2008]. The model has fully compressible non-hydrostatic equations and used mass-based terrain-following coordinate system. The

upper boundary has an absorbing layer Rayleigh relaxation, and implicit gravity wave damping.

The selection of the spatial domain was dictated by our requirement to simulate convection over Central Indian landmass and over BoB. Fig 1 shows the domain of simulation with the most important geographical features of the region. The primary simulation which is capable of simulating the southward propagations at a CRM resolution of 3 km with explicit microphysics was run for the duration of June to August of 2008 over the Indian region. The simulation has 1000 x 1000 grid points in the horizontal and 100 levels in the vertical with an eta-coordinate system. The horizontal grids follow Arakawa C-grid staggering [Arakawa and Lamb, 1977] and the vertical grid spacing varies with height. The lateral boundary conditions for the model are specified with relaxation zone of 4 grid points. The initial condition and the boundary conditions (updated every 6 hours) are from the NCEP FNL (Final) analysis dataset (Operational Global Analysis).

In the explicit simulation we use the single moment class-3 (WSM3) microphysics scheme by Hong et al [2004]. This scheme treats water vapor, cloud water, and rain water mixing ratio above 0°C and water vapor, ice water, and snow water mixing ratio below 0°C. The Yonsei University (YSU) scheme [Hong et al, 2006] is used to represent planetary boundary layer processes. The model time step is 5 seconds and the model output is archived every 3 hours.

As mentioned previously, the southward-propagating MCSs are missing from most coarse resolution general circulation model simulations and reanalysis data. To evaluate the presence of these MCSs in WRF we performed additional simulations at different horizontal resolutions and with explicit microphysics and Kain-Fritsch (KF) cumulus pa-

rameterization [Kain and Fritsch, 1993; Kain, 2004]. The different configurations used for this sensitivity study are summarized in Table 1. Apart from the control CRM simulation discussed above, a total of 7 simulations were carried out at varying horizontal and vertical resolutions and with different moist convection representation. Keeping all the physics options same as control, we changed the horizontal resolutions to 12 and 30 km for two simulations. The number of vertical levels were reduced to 50. These simulations were run with WSM3 microphysics (and no cumulus parameterization) for the month of June, 2008.

We carried out a simulation at a resolution of 3 km in which we used KF cumulus parameterization to show that KF assumptions break down at such finer resolution. Most of the high resolution reanalysis datasets are generated using both microphysics and cumulus parameterizations. We carried out two simulations at 12 and 30 km horizontal resolution (results are not shown in this paper) for June, 2008. In these simulations, we used both WSM3 microphysics and KF cumulus scheme. We found that contribution of microphysics to total precipitation was negligible compared to that by KF. Since cumulus parameterization dominates the total precipitation, we show the results of the simulation (at 12 and 30 km) using only KF in the following discussions. Using only KF (or only WSM3) in the simulation enables us to filter out the effects of microphysics (cumulus parameterization) on the simulated thermodynamics and dynamics of the simulated system. The distribution of precipitation between KF and microphysics in WRF at different horizontal resolutions has been throughly discussed in Duda [2011].

Duda [2011] found that for horizontal resolutions finer than 4km, microphysics schemes dominated cumulus parameterization in total precipitation. While for resolutions coarser

than 4km, cumulus parameterization dominated the total precipitation. We would have liked to carry out a simulation at 3 km where we used both KF and WSM3. However, due to computational cost involved we are showing results for simulations which used either WSM3 or KF exclusively, knowing well that the assumptions used in KF break down at such high resolution.

Many of these simulated MCSs initiated over land and propagated south over BoB. To study the role of diurnal land surface temperature variation in initiation of these MCSs, we switched off land surface temperature prediction in explicit microphysics case at 3 km and ran the model for the month of June. The rest of the physics schemes were kept same as that in primary CRM simulation (3Micro). Before delving into the southward propagations in the model, we evaluate the mean precipitation features.

3. Data Description and Methodology

To validate the simulated temporal and spatial features of the precipitation, we use the 3 hourly Tropical Rainfall Measuring Mission (TRMM) 3B42 version 7 data [Huffman et al, 2007]. TRMM 3B42 precipitation estimates are based on high quality microwave data, TRMM Precipitation Radar data, and rain gauge data. The horizontal resolution of the data is 0.25°. TRMM and model precipitation estimates are one and a half hour apart. For example a 9am time stamp on the TRMM data refers to precipitation between 7:30 to 10:30am. The model on the other hand calculates accumulated precipitation between time stamps. So, precipitation between 6am to 9am in the model will be calculated as the difference between the accumulated precipitation between these two time stamps and will be centered at 7:30am. To make both TRMM and model precipitation refer to the same time stamp, we have interpolated the TRMM precipitation estimates to model time. One

more thing to note is that we have carried out multiple model simulations at different resolutions. However, since the primary focus of this paper is the study of the southward propagating MCSs, we do not intend to calculate spatial correlation between observations and model data. Hence, we have not regridded any data.

4. Results

4.1. Mean Precipitation Features

During the monsoon, the moisture-laden south westerlies from the Indian Ocean carry moisture to the landmass. These winds are almost orthogonal to the coast and are blocked by Western Ghats which run parallel to the western coast (Fig 1). Much of this moisture is lost on the windward side due to orographic lift, giving large precipitation in the region. Fig 2 shows the monthly precipitation from the TRMM satellite estimates and from the model (3Micro) for the simulated period. Orographic precipitation on the windward side (west) of the Western Ghats can be seen in TRMM and in simulations. On the leeward side, the loss of moisture is evident as can be seen in both the TRMM and the simulation. Himalayan orography also interacts with moisture laden winds from BoB and the combination of land-sea heating contrast gives frequent episodes of precipitation over the foothills.

The model overestimates the precipitation over most of the Equatorial Indian Ocean (5°N) for all the months. In TRMM, the precipitation over the the Arabian Sea and BoB reduces while that over Central Indian landmass increases as the season progresses. The northward propagation of the tropical convergence zone (TCZ) plays a major role in modulating monsoon precipitation over south Asia [Sikka and Gadgil, 1980]. The TCZ sits near 5°N during 15 May to 15 June. It then starts propagating north. We believe that

the lower tropospheric winds and the location of TCZ thereof plays an important role in modulating southward propagation of MCSs. TRMM shows a lot of precipitation in the north BoB region. We will show in our sensitivity studies that most of this precipitation comes from diurnally-generated systems.

4.2. Equatorward Propagation of MCS

We analyzed TRMM data from 1998-2014 and found that the southward propagations were most prominent during the onset phase of the monsoon. Southward propagations were also found to be prominent during the month of June in the simulations (16 out of 17 years of data showed southward propagations). We show the latitude-time Hovmoller diagrams of the 3 hourly precipitation data from model and from TRMM averaged over 85 to 90°E for the month of June, 2008 in Fig 3.

A very distinct large-scale northward propagating precipitation signal can be seen in TRMM from 7 to 17 June. Embedded in this large-scale propagation are the mesoscale diurnal southward propagating precipitation episodes. The extent of these signals varies from less than 5 degrees for the smallest signal to more than 25 degrees for the largest signal seen on 5 June. This unbroken signal signifies a continuously propagating MCS originating on the coast north of BoB. The mean speed of this structure (approximately 15 m/s) cannot be explained solely by the mean tropospheric advection [Liu et al, 2008], but is similar to gravity wave speeds. The model simulations also show southward propagating diurnal precipitation episodes embedded within larger northward propagating rain band. The number of episodes is considerably higher in the model than in TRMM. The smallest signals span less than 5 degrees and the largest 15 to 20 degrees in the model simulation. In both the TRMM and the model these signals sometimes originate over the

coastal regions and sometimes over the Ocean. The duration of the simulated MCSs is opposite of observations with the shorter MCSs occurring first and the longer occurring later. Also, MCSs continue to form in the model after 15 June, but not in observations. When we analyzed 17 years of TRMM data, we found southward propagating MCSs embedded within northward propagating Intraseasonal envelop. The duration of the observed systems showed a large variability. For June 2008, the structure we found was like the one shown in Fig 3. We do not yet know why this was the structure for 2008. However, this is not uniform year after year. We also do not yet know why the MCSs stopped forming in TRMM but continued to form in the model after 15 June. We would like to explore the reasons behind these findings in a future study.

Figure 4 shows the model simulated 3 hourly precipitation for one of the propagating episodes. This episode occurred on 6 June (an isolated event) and was selected for further investigation. This precipitation signal originated at the coastal region north of BoB between 1430 to 1730 local time, intensified for the next three hours over the north BoB, and then started propagating southward in a bow structure. Comparing this with the radar echoes reported by Houze [2004], our model is able to simulate the structure of these precipitation events reasonably well. Fig 5 shows the maximum radar reflectivity in dBZ of the propagating MCS by the model as seen at 2030 hours on 6 June in Fig 4. The system comprises a leading convective/trailing stratiform bow structure and agrees well with the one reported in Webster et al [2002] and Houze [2004].

4.2.1. Determination of Origination and Direction of Propagation of the System

From Fig 3 we estimate that these systems propagate at speeds of about 15 m/s. The propagating system can be seen in Fig 4 to have originated over the coastal region north of the BoB at 23°N. In the model, the land surface temperature was updated 4 times in a day, while the sea surface temperature was updated only once a day. Hence, land has a strong diurnal cycle while ocean has none. The relationship between diurnal land surface temperature and precipitation maximum was studied by Kataoka and Satomura [2005] over the Meghalayan plateau (near Himalayan foothills north of the BoB). They reported that late night-early morning precipitation structure was a squall line which propagated southwards due to MCSs cold pool. In their conclusion, they speculated that these MCSs might be related to the systems reported in Webster et al [2002] and Zuidema [2003] which affected the diurnal cycle over the BoB. In our simulation we get systems which initiated over land and propagated south. However, since our domain is much larger than that used in Kataoka and Satomura [2005] both temporally and spatially, we also get systems which initiated over ocean and started propagating south. Later in this study we will see how far the MCSs initiated over land affect precipitation over the BoB.

The diurnal cycle in surface temperature over the land is shown in Fig 6. Maxima in land temperature occurs late in the afternoon and the precipitation over land can be first seen at 830 local time in Fig. 4 and by the time of maximum surface temperature (1430 in the Fig. 6), we see a mature precipitating system (20°N in Fig. 4). It is interesting to note that the system intensifies when the land surface is warmer than Ocean. This system forms a bow structure and starts propagating south from 1730 local time onwards.

The investigation of the propagating system can be divided into determination of the direction of propagation and the speed of propagation. The direction of propagation was

attributed to the presence of surface to 600 hPa wind shear by Miyakawa and Satomura [2006]. However, Liu et al [2008] concluded that the direction of propagation was orthogonal to the mean advection and there was no steering level.

Miyakawa and Satomura [2006] showed seasonal mean 600 hpa winds to have a southward component. Figure 7 shows mean of model simulated 600 and 850 hPa wind speed for the month of June. 850 hPa winds are orthogonal to the direction of propagation, however at 600 hPa, it can be seen that the horizontal winds have south-eastward component over the the region of interest (85-90°E). These winds are in the direction of propagation. These winds were attributed by Miyakawa and Satomura [2006] to the trough over the BoB at the height of 600 hPa. We analyzed winds in many reanalysis datasets (not shown in this paper) and found mid-tropospheric southward winds during the onset phase of the monsoon. We also analyzed winds at all the levels in our model simulation and found the mid tropospheric winds (from 700 to 500 hPa) to be in the direction of propagations. The mean magnitude of 600 hPa winds (10 m/s) during June, however, was lower compared to the overall speed of the propagating MCS (15 m/s) and Miyakawa and Satomura [2006] speculated that the discrepancy may be attributed to rebuilding of convective cells provoked by cold pool outflows. To understand the discrepancy in speeds, we analyzed vertical cross sections of these MCSs. It is important to mention here that in the following discussion, though we are analyzing an MCS which occurred prior to large scale northward propagation, structure of all MCSs during a northward-propagating episode were similar.

In Fig 8 and Fig 9 we show the cross-sectional plot of equivalent potential temperature, meridional wind vectors, cloud water mixing ratio and rain water mixing ratio of the propagating episode shown in Fig 4 along the line shown in Fig 5. In Fig 8 the surface to 875

hPa height meridional winds have northward component whereas the mid-tropospheric winds (700 to 500 hPa) have a southward wind component. Figure 8 shows the initiation phase of convection while Fig 9 shows the mature phase of convective system which propagates south. It can be seen in Fig 8 that initially, the surface is warmer compared to the mid-troposphere. As the day progresses, the surface gets warmer still. A deep convective cloud is formed at 1430 local time. As this system matures and starts precipitating (rain water mixing ratio shown by the black contour in the Figure 9), it gives rise to convective downdrafts driven by the evaporation of precipitating rain water. As these downdrafts hit the ground and encounter warm surface winds, a front like structure forms (at 20.6°N). It can be seen that the convective system is intense and possesses a strong downdraft which creates a density current.

4.2.2. Speed of Propagation

In Fig 10 we show the meridional wind velocities (greater than 5 m/s) and vertical wind velocities (greater than 1 m/s) for the system. The southward winds behind the system is the rear inflow jet and can be clearly seen. It can also be seen that speed of rear inflow jet near the surface (surface to 875 hPa) is around 15 m/s which is the speed of propagation of this MCS. It is important to note that although we are showing the rear inflow jet only near the surface, the rear inflow jet has a vertical extent spanning from surface to mid-troposphere.

The propagating system velocity can be divided into advective component and cloud scale velocities in a way described in Corfidi et al [1996] and Corfidi [2003]. The advective component is the mean of cloud layer usually taken from 850 to 300 hPa height and the cloud scale velocities come from cold pool associated with downdraft and the low-level

jet (maximum incoming velocity in 500m to 1km). According to Corfidi et al [1996], an estimate of the propagation speed is the vector sum of advective component (or cloud layer velocity) and the negative of low-level jet, while according to Corfidi [2003], an estimate of the propagation speed is the vector sum of cloud scale velocity (or cold pool velocity) and the negative of low-level jet. We need to quantify these properties for our system.

If one looks closely in Fig 10, one can see that the associated updraft-downdraft pair is akin to Fig 2. of Moncrieff [1992] which features the hydraulic jump-like system characterized by inflow from ahead of the system (i.e., strictly propagating system without a steering-level) which might be the salient dynamical model of the BoB systems, as also found in Liu et al [2008]. Also, there are upward displacements of the conserved θ_e ahead of the system giving rise to initiation of new convective cell. This upward displacement of θ_e must indicate clear-air lifting, which would indeed be the mechanism of gravity wave coupling. Indeed, gravity currents are important in the continual initiation of convection at the leading-edge (southward side) that keeps the MCSs alive for long periods.

Figure 11 top panel shows the near surface anomaly of equivalent potential temperature of the episode at 2330 hours on 6 June. The anomaly is calculated by taking difference from when the system was not present i.e. at the exact location in this Figure 6 hours back. Fig 11 also shows the perturbation pressure (central panel) and absolute temperature values for the system. The downdraft associated cold pool is clearly visible on the lower right corner having negative θ_e anomaly. In this cold pool region, the mean meridional speed was found to be 15.2 m/s. The warmer air can be seen to be lifted up by this cold pool to the lifting condensation level (LCL, which in this case was around 500 to 600m, or around 975 to 950 hPa). The mean wind below the LCL ahead of the system was found to be

1.5 m/s. So, one can argue that the convection initiation zone would be moving at the speed of around 15 m/s, which is indeed the case. Hence, the propagation of this MCS is indeed governed by gravity current mechanism.

To a first theoretical approximation, we can use the following equation [Simpson, 1997] to derive gravity current speed in atmosphere

$$u = \sqrt{gh\Delta T/T} \tag{1}$$

where u is the propagation speed of gravity current, h is the depth of density current (500m to 1km), T is the environmental air temperature and ΔT is the air temperature difference of cold pool from environment. The depth of cold pool in our simulation is around 700m to 1km. The temperature difference is around 5 to 10K, and the environmental air temperature is 300K. Then the gravity current speed is in the range of 12 to 18m/s.

A better understanding of the environmental contribution to the propagation of the MCSs comes from Corfidi et al [1996] and Corfidi [2003] approach. As discussed earlier, we divide contribution to overall propagation into advective component (900 to 350 hPa in our case), contribution from low-level jet (990 to 960 hPa ahead of the system), and the cold pool. Figure 12 shows equivalent potential temperature averaged over 990 to 960 hPa, the low-level velocities (averaged over 990 to 960 hPa) associated with cold pool and low-level jet, and the cloud scale velocities (averaged over 900 to 350 hPa). Figure 12 also shows the leading edge of convergence at 975 hPa. We can see that the cold pool produces outflow boundaries. These outflows lift the warm south-westerlies to form new convective cells. The leading edge does move in the direction of vector sum of the cloud layer velocity (or cold pool velocity) and the negative of low-level jet.

Given the fact that the size of the interface of cold air and warm air and that of convective core itself is nearly 30 km, we ought to ask whether the simulation of propagating system depends on the resolution. So are the present day cumulus parameterization schemes, which are designed for non-hydrostatic mesoscale models (like WRF here) capable of simulating these observed equatorward propagating systems? To answer these questions, we carried out a number of simulations by varying the horizontal resolution in the model while keeping the physics and dynamics schemes same in the model. In addition to these, we carried out experiments in which the resolution in the model is varied and instead of using an explicit microphysical scheme, we use Kain-Fritsch cumulus parameterization scheme.

4.3. Effects of Convection Scheme and Resolution

Figure 13 shows the precipitation simulated by the various physics and resolution configurations in the model shown in Table 1. Let us first discuss the effect of changing the horizontal resolution in the simulation. Similarities exist between the different resolutions using the same convection representation. In simulations using microphysics, all the resolutions get higher western ghats precipitation and all the resolutions over-precipitate over ocean and under-precipitate on land compared to TRMM estimates shown in Fig. 2. It can be seen in Fig 13 that much finer structures are resolved by the microphysics case compared to cumulus case. The rainfall is overestimated by the coarser resolution microphysics cases (12Micro and 30Micro). However, the large scale features are very similar between the different resolutions.

The simulations differ substantially when we use cumulus parameterization instead of microphysics. The simulated rainfall is not substantially different between the resolutions

(3Cu, 12Cu, and 30Cu). The KF cumulus parameterization used in the simulation uses large scale vertical velocity at the lifting condensation level to initiate convection. The closure in the model is based on the adjustment of Convective Available Potential Energy (CAPE) depending on an adjustment time scale to ensure smooth interaction between synoptic scale and cumulus scale. Also, in KF, the transports of cloud mass in a model column is carried out using updrafts, downdrafts, and environmental large scale mass fluxes till 90% of the CAPE is consumed. Hence the convection is more likely to occur in the regions of higher CAPE. We found that in the simulations using cumulus parameterization, CAPE was high everywhere (not shown in this paper) and hence KF triggered convection frequently everywhere. The resulting precipitation can be seen in the Fig 13 where we find precipitation over most of the domain. Compared to TRMM precipitation, the cumulus case performs exceptionally poorly. It does not get any fine scale features seen in TRMM as well as in microphysics simulation.

Figure 14 shows the time-latitude plot of the precipitation over BoB with different model resolution and convection representation shown in Table 1. A strong diurnal cycle of precipitation can be seen in all the simulations. Also, it can be seen that the southward propagations in the model are resolution dependent as well as on the convection representation. In the 12Micro and 30Micro case, the propagations are nearly absent or the precipitation system is not continuous as in 3Micro case. For a few of the intense precipitating systems, 12Micro and 30Micro were able to resolve the updraft-downdraft pair for a short duration but could not continue to resolve the pair for long. We can attribute the failure of coarser resolution model simulation to the fact that propagation in the model requires correct simulation of updraft-downdraft pair and the associated

circulation. As we have seen, the size of the convective core is nearly 30 km, the 12Micro and 30Micro cases might fail to simulate this fine scale interaction between this core and downdraft happening in the boundary layer. While in microphysics case the precipitation structures are sharp, the precipitation signal in the cumulus parameterization case are much smoother. In all the simulations with cumulus parameterization (3Cu, 12Cu, and 30Cu), the southward propagations are absent. The systems in microphysics case tend to move south near the Himalayan foothills (north of 20°N) while those in cumulus parameterization case move north.

Figure 15 shows the vertical cross section of the equivalent potential temperature, meridional and vertical wind vectors for the non-propagating system in 3Cu case. Note that cloud microphysical variables such as cloud water mixing ratio and rain water mixing ratio are absent in the cumulus case. The surface to mid-tropospheric winds simulated by the cumulus case are northwards. It can also be seen that most of the convection in the cumulus case is initiated due to orographic lift by Himalayas. Cumulus parameterization assumes that the model grid is large enough to have updraft and downdraft inside the grid box, whereas in the microphysics case, true sources of heating-cooling and eddy transports (local and non-local) are calculated explicitly. Hence, high resolution model with microphysics is able to simulate updraft-downdraft pair which is missing in cumulus case.

Figure 16 top two panels show heating and cooling tendencies of a precipitating system in 3Cu vs. 3Micro case. Heating tendency is calculated by taking difference between equivalent potential temperature when the system is present and when there was no system at the location 6 hours back. Most of the heating in 3Cu case happens in mid-to

upper troposphere. A very strong low-level cooling and a gravity current can be seen in 3Micro case. The cooling of the lower troposphere in 3Cu is also present. But it is not as strong as the one seen in 3Micro case.

Figure 16 lower panel shows the mean meridional momentum tendency horizontally averaged for the system shown in the top two panels. It can be seen that the MCS in 3Micro case has a strong southwards tendency in the lower troposphere. We took mean of wind speeds in the cold pool in Fig 11, we found that the mean wind in the cold pool (lower right corner) was 15.2 m/s. While the northward winds in the lower troposphere were 1.5 m/s (lower left corner). We can see in Fig 16 that the initiation of convection is happening due to density current-like structure traveling in the southwards direction.

The BoB presents a very unique problem for cumulus parameterizations based on mass flux schemes using CAPE closure. As mentioned previously, we found that in our simulations, CAPE values were always very high over the BoB. Also, BoB has a lot of precipitable water. This resulted in poor simulation of precipitation in 3, 12, and 30Cu cases. Similarly, the general circulation models using CAPE closure in cumulus parameterization tend to trigger frequent local precipitation. In addition it is difficult for a General Circulation Model to correctly predict precipitation from MCSs which propagate from land to over the BoB. Moncrieff and Liu [2006] have pointed out many shortcomings of the present day cumulus parameterizations. It can be said that the mesoscale non-hydrostatic models suffer because of the fact that there is no proper convection representation available in the grey area of parameterization (5 to 30 km horizontal resolution). Using only microphysics at coarser resolution is problematic because microphysics has to create grid size saturation. This implies that a grid size of 30 km would either be completely saturated

or unsaturated which is not always true. Similarly, using cumulus parameterizations at these resolutions is also not correct because of the inability of parameterizations to adapt to varying horizontal resolutions. Organized MCSs are not represented in cumulus parameterization [Randall et al, 2003]. Attempts are being made to include all the above mentioned processes in the parameterizations [Yano and Moncrieff, 2016] for model horizontal resolutions in the grey scale (5 to 30 km).

At the end of this study, we carried out one additional simulation in which we kept the land surface temperature constant for the month of June while keeping the rest of the physics options and model resolution same as 3Micro. Figure 17 shows the simulated precipitation and southward propagations in this simulation. Taking the difference of precipitation from our primary simulation (with diurnal land temperature variation) shows that most of the north BoB precipitation comes from systems originating over land. This can be verified by looking at the southward propagation in this simulation. The southward propagations are missing from this simulation in north BoB though there are MCSs which initiated over ocean and propagated south. When a system initiates over ocean, it produces cold pool outflows and results in MCSs formation. According to Corfidi [2003], an MCS will move in the downwind direction because it is the direction of most intense convergence. Over BoB, this happens to be the southward direction.

5. Conclusions

In the present study, we performed a season long WRF simulation of the South Asian Monsoon at 3 km horizontal resolution with explicit microphysics scheme to study the southward propagating MCSs over the BoB. The simulated structure of the southward propagating MCSs agrees well with the one previously reported in observations. Simulated

episodes show leading line/trailing stratiform MCSs which propagate southwards at the speed of 15-20 m/s. The system initiates over land during the day time due to land-sea temperature contrast and initiate offshore at night. These MCSs propagate south inside the northward propagating intraseasonal oscillations.

The model correctly simulates the 600 hPa southward winds which were reported in a previous study and are believed to contribute to the advective component to MCSs propagation. The simulation shows that the velocity of the rear inflow jet near the surface is similar to the propagation speed of MCS. A simple density current model applied to the boundary layer under the convective region shows change in momentum in the direction of propagation. The vector sum of either the rear inflow jet velocity (averaged over 990 to 960 hPa) or the advective component of cloud layer (mean wind in 900-350 hPa layer) and the negative of low-level jet (average of 990 to 960 hPa winds ahead of the system) have been used in previous studies to derive the velocity of maximum convergence zone and that of the MCSs in general. In our simulations, we found this to be true for the southward propagating MCSs.

The correct representation of convection initiation, both by diurnal land heating and due to updraft-downdraft pair is necessary to produce gravity current structure characteristic of these MCSs. The simulation of the propagations is sensitive to the horizontal resolution in the model. The horizontal extent of the convective updraft and the downdraft is 30 km. Most of the high resolution reanalysis datasets are generated using both microphysics and cumulus parameterizations. We carried out two simulations at 12 and 30 km horizontal resolution (results were not shown in this paper) in which we used both WSM3 microphysics and KF cumulus scheme. We found that southward propagations

were missing from these simulations and contribution of microphysics to total precipitation was negligible compared to that by KF. Since cumulus parameterization (KF) dominated the total precipitation, we subsequently carried out simulations in which we used either KF or WSM3 microphysics exclusively at 3, 12, and 30 km horizontal resolutions to see which of the convection representation (KF or WSM3) was causing the failure of model in simulating the southward propagations. The model at 12 km horizontal resolution and using only microphysics was sometimes able to simulate the updraft-downdraft pair of this MCS and hence the southward propagations. The model at 30 km horizontal resolution using only microphysics was hardly able to resolve this pair and even when it did, it was unable to maintain that feature for southward propagations to persist.

These propagations are missing in the simulations using cumulus parameterization instead of explicit microphysics. In simulations using cumulus parameterization, it is seen that most of the convection is initiated due to orographic lift by Himalayas. The heating and cooling due to updraft and downdraft seen in microphysics case is missing in cumulus case because the cumulus parameterization has only local responses to heating and cooling as opposed to non-local heating in the microphysics case. The cumulus parameterization produces heating in the mid-troposphere and no cooling near the surface due to precipitation. The cooling due to precipitation plays an important role in creating the gravity current structure characteristic of the southward propagating MCSs.

Also essential to simulating these MCSs is the diurnal land heating cycle which is responsible for initiation of MCSs over land. When we switched off this diurnal land heating for the month of June, the MCSs disappeared from the northern BoB. However, the MCSs were present over south BoB. These MCSs were initiated over ocean. This

indicates that the wind shear structure is favorable for southward propagation. But, since land diurnal heating was switched off, no initiation happened for these MCSs over land. Taking the difference of precipitation from our primary simulation (with diurnal land temperature variation) showed that most of the north BoB precipitation came from systems originating over land.

The resolution between explicitly resolving convection (as in CRMs) and heavily parameterized cases (as in cumulus parameterization for General Circulation Models) is the grey area in parameterization and is a deadlock in convection representation in numerical weather prediction models [Arakawa and Wu, 2013; Wu and Arakawa, 2014]. The mesoscale non-hydrostatic models suffer from the fact that there is no proper convection representation available in the grey area of parameterization(5 to 30 km horizontal resolution). Using only microphysics at coarser resolution is problematic. Similarly, using cumulus parameterizations at these resolutions is also not correct because of all the complexities of convection happening at this resolution and the inability of parameterizations to adapt to varying horizontal resolutions. We can say that future convection schemes should be able to transform themselves smoothly as the resolution of the model is changed. The model should be able to simulate mesoscale propagations even at coarser resolution.

Acknowledgments. The TRMM satellite precipitation estimates data used in this study can be found at https://mirador.gsfc.nasa.gov/collections/TRMM_3B42_daily__007.shtml The WRF model data is available with the authors and can be made available on request. Since the data is huge, subsets will be made available on request. For funding we would like to acknowledge National Monsoon Mission, INCOIS. There are no real or perceived financial conflicts of interests for any author.

References

Arakawa A, Lamb VR (1977) Computational design of the basic dynamical processes of the ucla general circulation model. Methods in computational physics 17:173–265

Arakawa A, Wu CM (2013) A unified representation of deep moist convection in numerical modeling of the atmosphere Part I. Journal of the Atmospheric Sciences 70(7):1977–1992

Boos WR, Kuang Z (2010) Mechanisms of poleward propagating, intraseasonal convective anomalies in cloud system-resolving models. Journal of the Atmospheric Sciences 67(11):3673–3691

Chakraborty A, Nanjundiah RS, Srinivasan J (2009) Impact of african orography and the indian summer monsoon on the low-level somali jet. International Journal of Climatology 29(7):983–992

Chakraborty A, Nanjundiah RS (2012) Space–time scales of northward propagation of convection during boreal summer. Monthly Weather Review 140(12):3857–3866

Chattopadhyay R, Goswami B, Sahai A, Fraedrich K (2009) Role of stratiform rainfall in modifying the northward propagation of monsoon intraseasonal oscillation. Journal of

Geophysical Research: Atmospheres 114(D19)

Choudhury AD, Krishnan R (2011) Dynamical response of the south asian monsoon trough to latent heating from stratiform and convective precipitation. Journal of the Atmospheric Sciences 68(6):1347–1363

Corfidi S, Meritt J, Fritsch J (1996) Predicting the movement of mesoscale convective complexes. Weather and Forecasting 11(1):41–46

Corfidi SF (2003) Cold pools and mcs propagation: Forecasting the motion of downwind-developing mcss. Weather and Forecasting 18(6):997–1017

National Centers for Environmental Prediction,National Weather Service,NOAA,U.S. Department of Commerce, NCEP FNL Operational Model Global Tropospheric Analyses continuing from July 1999, https://doi.org/10.5065/D6M043C6, Research Data Archive at the National Center for Atmospheric Research, Computational and Information Systems Laboratory, Boulder, Colo. (Updated daily.) Accessed 01 01 2017.

DeMott CA, Stan C, Randall DA, Kinter III JL, Khairoutdinov M (2011) The asian monsoon in the superparameterized CCSM and its relationship to tropical wave activity. Journal of Climate 24(19):5134–5156

Gadgil S (2003) The indian monsoon and its variability. Annual Review of Earth and Planetary Sciences 31(1):429–467

Gadgil S, Gadgil S (2006) The indian monsoon, gdp and agriculture. Economic and Political Weekly pp 4887–4895

Gambheer AV, Bhat GS (2000) Life cycle characteristics of deep cloud systems over the indian region using INSAT-1B pixel data. Monthly Weather Review-USA 128(12):4071–4083

Gambheer AV, Bhat GS (2001) Diurnal variation of deep cloud systems over the indian region using INSAT-1B pixel data. Meteorology and Atmospheric Physics 78(3-4):215–225

Goswami BN, Ajaya Mohan R (2001) Intraseasonal oscillations and interannual variability of the Indian summer monsoon. Journal of Climate 14(6):1180–1198

Guhathakurta P, Rajeevan M, Sikka D, Tyagi A (2015) Observed changes in southwest monsoon rainfall over india during 1901–2011. International Journal of Climatology 35(8):1881–1898

Duda JD (2011) WRF simulations of mesoscale convective systems at convection-allowing resolutions. Iowa State University

Hong SY, Dudhia J, Chen SH (2004) A revised approach to ice microphysical processes for the bulk parameterization of clouds and precipitation. Monthly Weather Review 132(1):103–120

Hong SY, Noh Y, Dudhia J (2006) A new vertical diffusion package with an explicit treatment of entrainment processes. Monthly Weather Review 134(9):2318–2341

Houze RA (2004) Mesoscale convective systems. Reviews of Geophysics 42(4). RG4003

Huffman GJ, Bolvin DT, Nelkin EJ, Wolff DB, Adler RF, Gu G, Hong Y, Bowman KP, Stocker EF (2007) The trmm multisatellite precipitation analysis (tmpa): Quasi-global, multiyear, combined-sensor precipitation estimates at fine scales. Journal of hydrometeorology 8(1):38–55

Kain JS (2004) The kain-fritsch convective parameterization: an update. Journal of Applied Meteorology 43(1):170–181

Kain, John S., and J. Michael Fritsch (1993). "Convective parameterization for mesoscale models: The Kain-Fritsch scheme." The representation of cumulus convection in numerical models. American Meteorological Society. 165-170.

Kataoka A, Satomura T (2005) Numerical simulation on the diurnal variation of precipitation over northeastern bangladesh: A case study of an active period 14-21 june 1995. Sola 1:205–208

Krishnamurthy V, Goswami B (2000) Indian monsoon-ENSO relationship on interdecadal timescale. Journal of Climate 13(3):579–595

Lau K, Yang G, Shen S (1988) Seasonal and intraseasonal climatology of summer monsoon rainfall over east asia. Monthly Weather Review 116(1):18–37

Liu C, Moncrieff MW, Tuttle JD (2008) A note on propagating rainfall episodes over the bay of bengal. Quarterly Journal of the Royal Meteorological Society 134(632):787–792

Mapes BE, Warner TT, Xu M (2003) Diurnal patterns of rainfall in northwestern south america. part iii: Diurnal gravity waves and nocturnal convection offshore. Monthly Weather Review 131(5):830–844

Markowski P, Richardson Y (2011) Mesoscale meteorology in midlatitudes, vol 2. John Wiley & Sons

Medina S, Houze RA, Kumar A, Niyogi D (2010) Summer monsoon convection in the himalayan region: Terrain and land cover effects. Quarterly Journal of the Royal Meteorological Society 136(648):593–616

Miyakawa T, Satomura T (2006) Seasonal variation and environmental properties of southward propagating mesoscale convective systems over the bay of bengal. SOLA 2:88–91

Moncrieff M, So D (1989) A hydrodynamical theory of conservative bounded density currents. Journal of Fluid Mechanics 198:177–197

Moncrieff MW (1992) Organized convective systems: Archetypal dynamical models, mass and momentum flux theory, and parametrization. Quarterly Journal of the Royal Meteorological Society 118(507):819–850

Moncrieff MW, Liu C (2006) Representing convective organization in prediction models by a hybrid strategy. Journal of the atmospheric sciences 63(12):3404–3420

Nakazawa T (1988) Tropical super clusters within intraseasonal variations over the westren pacific. JMeteor Soc Japan 66(6):823–839

Randall D, Khairoutdinov M, Arakawa A, Grabowski W (2003) Breaking the cloud parameterization deadlock. Bulletin of the American Meteorological Society 84(11):1547–1564

Romatschke U, Houze Jr RA (2011) Characteristics of precipitating convective systems in the south asian monsoon. Journal of Hydrometeorology 12(1):3–26

Sahany S, Venugopal V, Nanjundiah RS (2010) Diurnal-scale signatures of monsoon rainfall over the indian region from trmm satellite observations. Journal of Geophysical Research: Atmospheres 115(D2)

Sikka D, Gadgil S (1980) On the maximum cloud zone and the itcz over indian, longitudes during the southwest monsoon. Monthly Weather Review 108(11):1840–1853

Simpson JE (1997) Gravity currents: In the environment and the laboratory. Cambridge university press

Skamarock WC, Klemp JB (2008) A time-split nonhydrostatic atmospheric model for weather research and forecasting applications. Journal of Computational Physics 227(7):3465–3485

Tulich SN, Kiladis GN (2012) Squall lines and convectively coupled gravity waves in the tropics: Why do most cloud systems propagate westward? Journal of the Atmospheric Sciences 69(10):2995–3012

Virts KS, Houze Jr RA (2016) Seasonal and intraseasonal variability of mesoscale convective systems over the south asian monsoon region. Journal of the Atmospheric Sciences 73(12):4753–4774

Wang B (2006) The asian monsoon. Springer Science & Business Media

Wang B, Fan Z (1999) Choice of south asian summer monsoon indices. Bulletin of the American Meteorological Society 80(4):629–638

Webster P, Bradley EF, Fairall C, Godfrey J, Hacker P, Houze Jr R, Lukas R, Serra Y, Hummon J, Lawrence T, et al (2002) The jasmine pilot study. Bulletin of the American Meteorological Society 83(11):1603–1630

Wu CM, Arakawa A (2014) A unified representation of deep moist convection in numerical modeling of the atmosphere part ii. Journal of the Atmospheric Sciences 71(6):2089–2103

Yano JI, Moncrieff MW (2016) Numerical archetypal parameterization for mesoscale convective systems. Journal of the Atmospheric Sciences 73(7):2585–2602

Zuidema P (2003) Convective clouds over the bay of bengal. Monthly Weather Review 131(5):780–798

Table 1.

Simulation Details					
Case Name	Horizontal Resolution	Number of Vertical levels	Microphysics	Cumulus Parameterization	Simulation Duration
3Micro	3 km	100	WSM3	None	June to August
3Cu	3 km	100	None	Kain-Fritsch	June
12Micro	12 km	50	WSM3	None	June
12Cu	12 km	50	None	Kain-Fritsch	June
30Micro	30 km	50	WSM3	None	June
30Cu	30 km	50	None	Kain-Fritsch	June
12MicroCu	12 km	50	WSM3	Kain-Fritsch	June (not shown)
30MicroCu	30 km	50	WSM3	Kain-Fritsch	June (not shown)

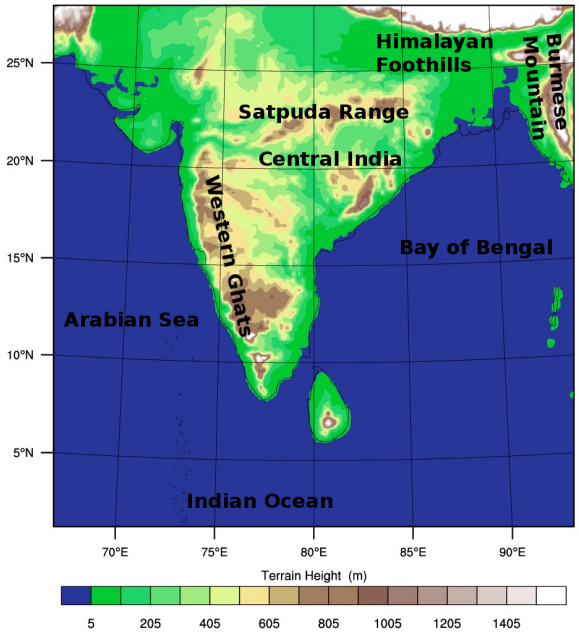

Figure 1. Model Domain showing orographic elevation and important geographical regions in Indian Sub-continent.

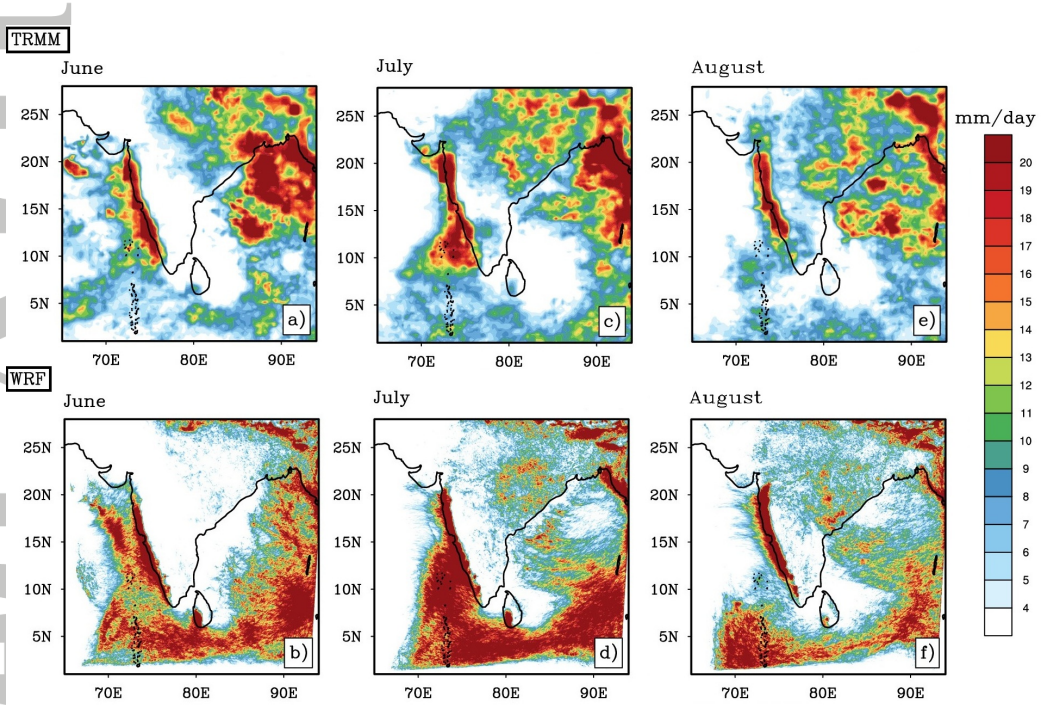

Figure 2. June-August monthly precipitation (mm/day) from TRMM satellite estimates and from model simulations (3Micro). Panels a, c, and e are from TRMM while b, d, and f are from model.

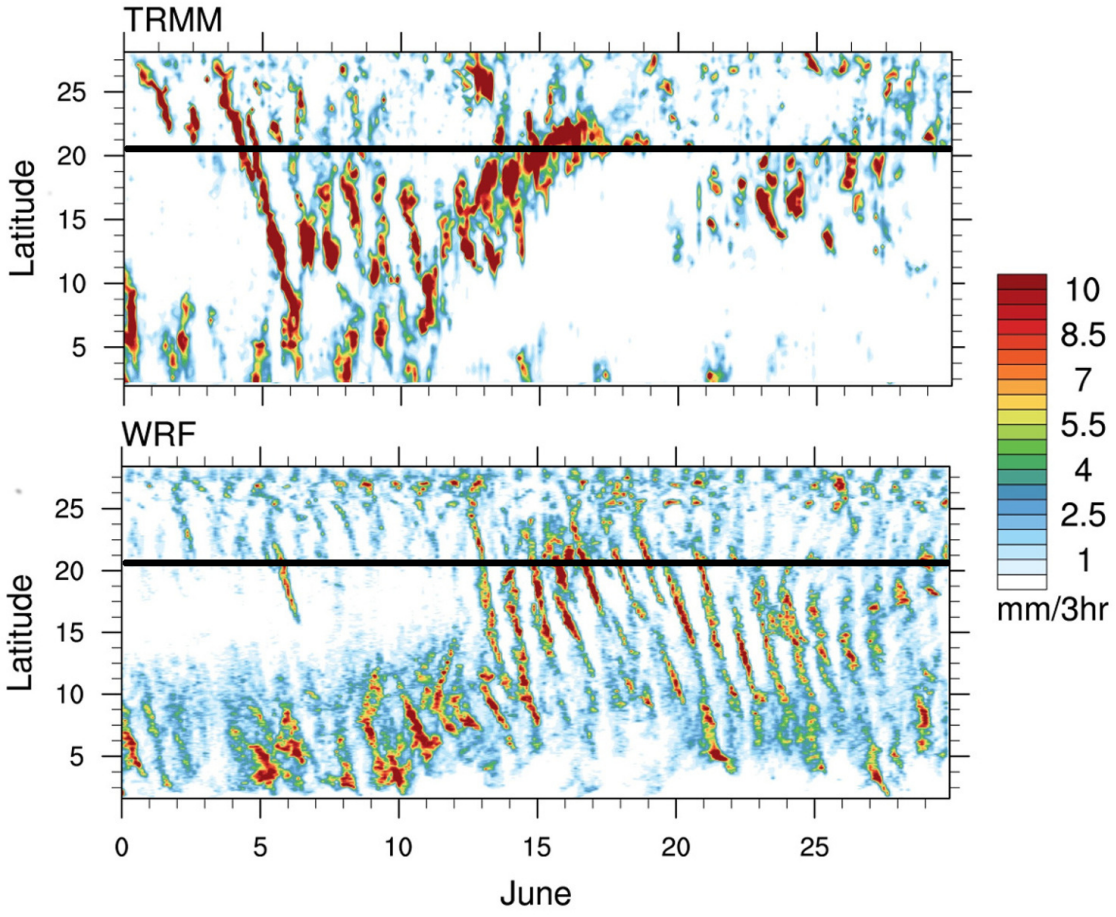

Figure 3. Latitude-Time Hovmoller plot of observed (TRMM) and modeled (WRF, 3Micro) precipitation averaged over 85-90°E showing diurnally propagating signals over the BoB. The horizontal line refers to mean coastline over 85-90°E. The southern tip of India is at 7°N.

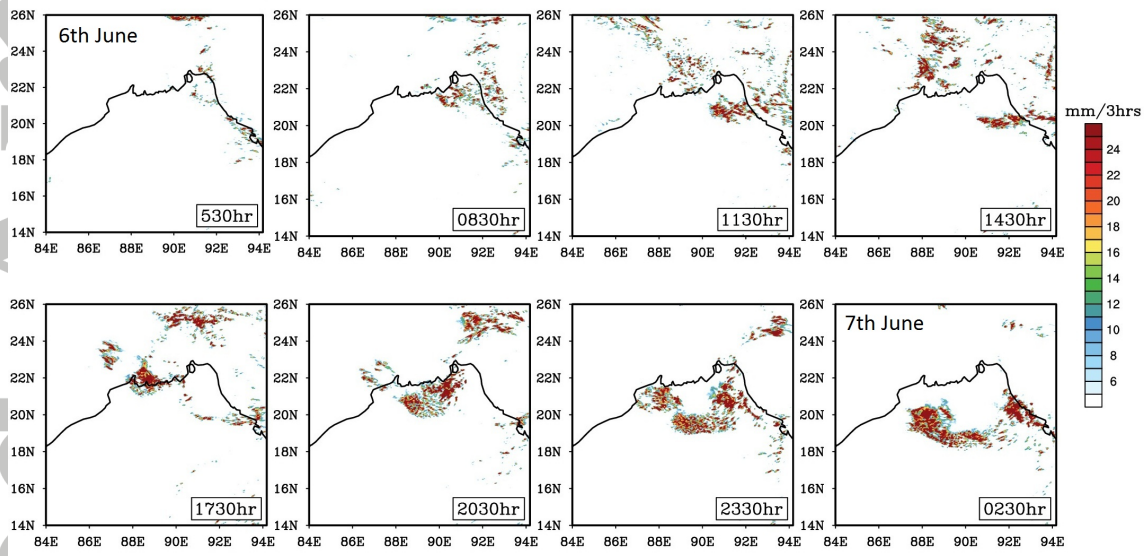

Figure 4. Particular precipitation episode (near 20°N-90°E) from model simulation propagating south. The system can be seen to have curved bow structure. The label on the right-down corner of each panel represents Local time on 6 June at which these snapshots were taken.

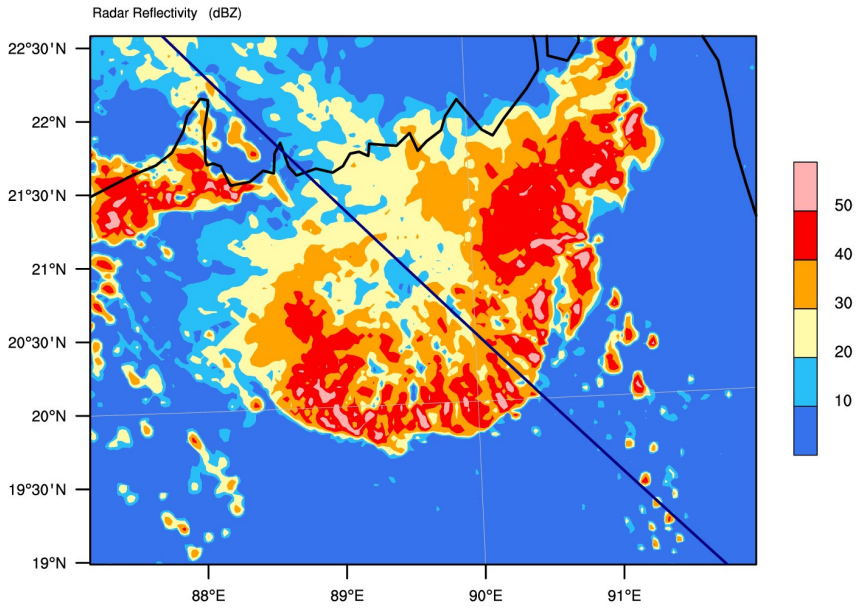

Figure 5. Time snapshot (at 2030 Local time on 6 June, 2008) of the maximum model simulated (radar) reflectivity (dBZ) of the propagating rain band. The inclined black line refers to the section along which the vertical dynamic and thermodynamic conditions are further analyzed.

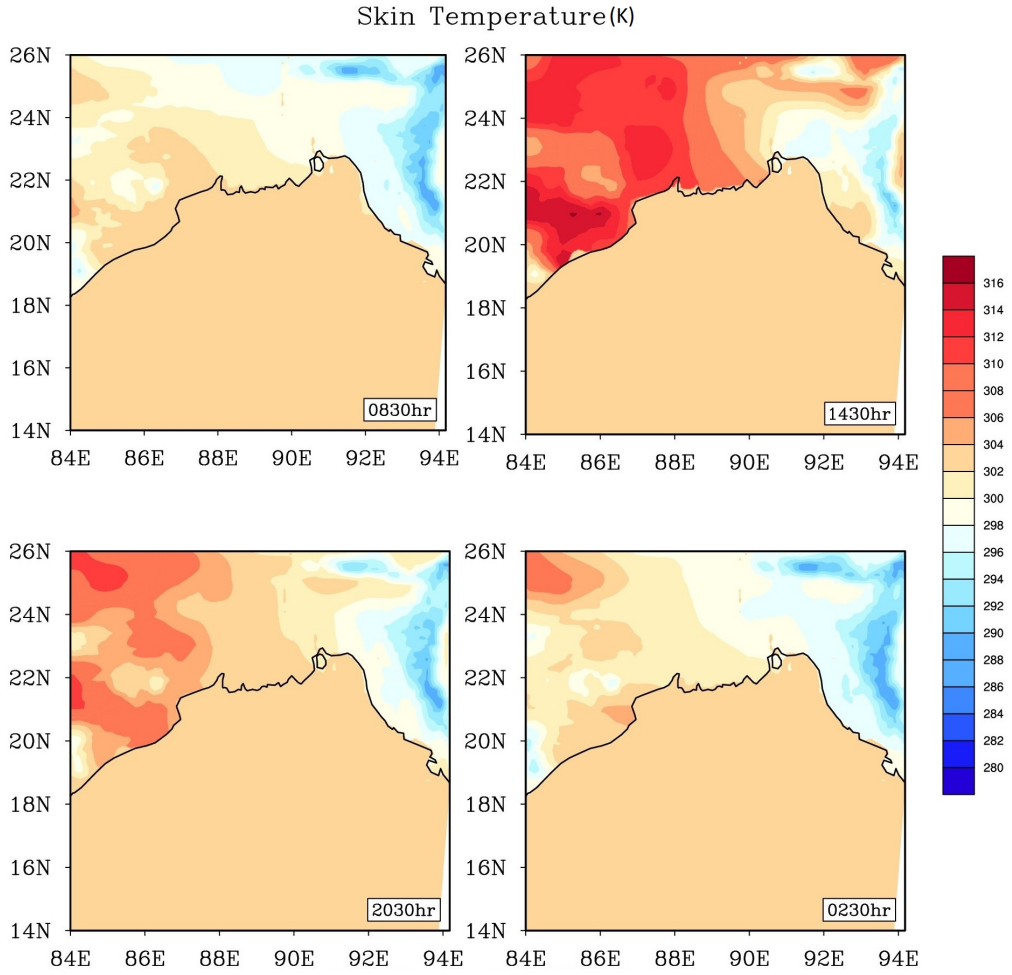

Figure 6. Surface temperature corresponding to the event shown in Fig 4.

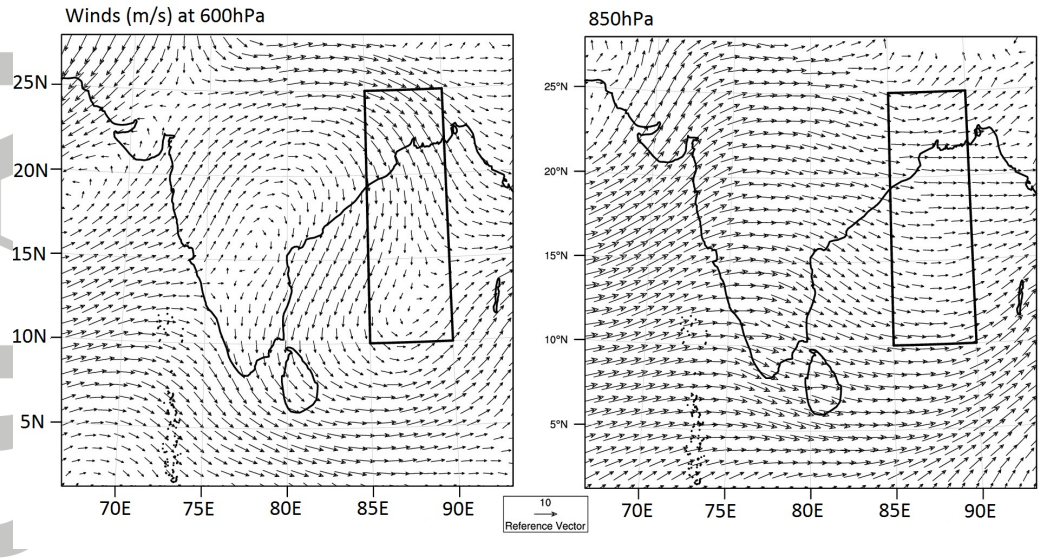

Figure 7. Monthly mean (June) model simulated horizontal winds at 600 and 850 hPa.

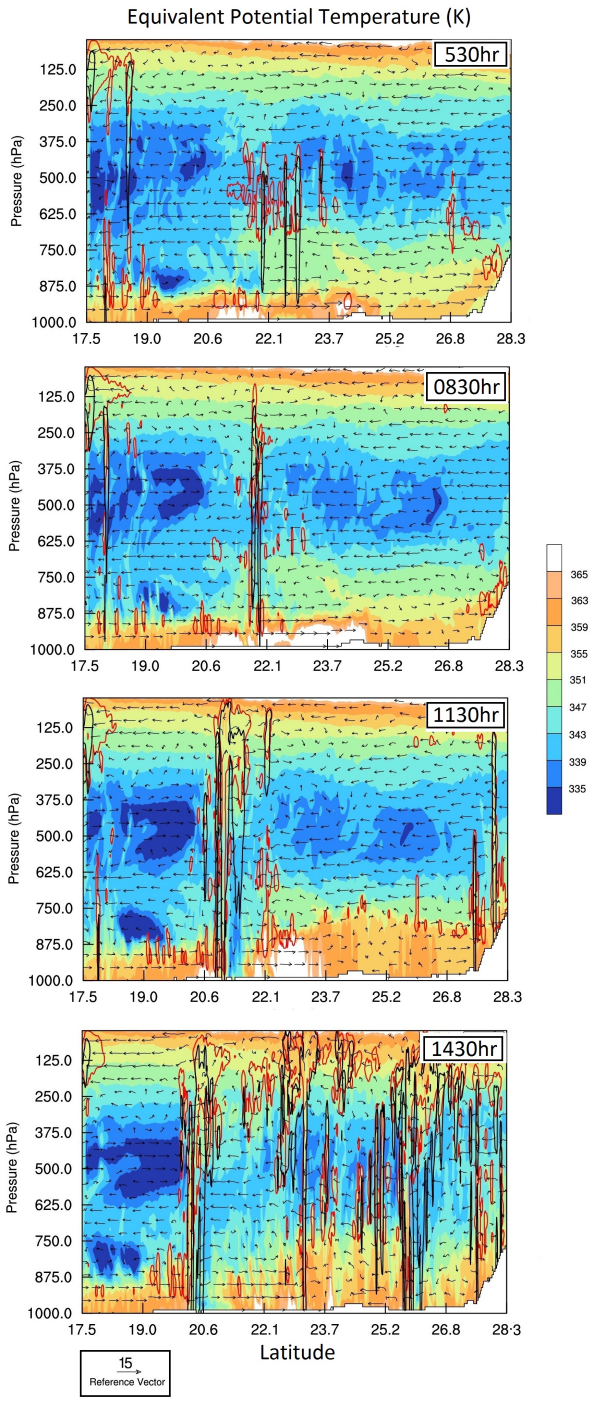

Figure 8. Cross-section plots along the black line shown in Fig 5 every three hours (local time on top right corner) showing the initiation of convection with equivalent potential temperature (color shaded), cloud water mixing ratio (red contour at 0.01g/kg), rain water mixing ratio (black contour at 0.3g/kg) and meridional winds (vectors (m/s)) for the event shown in Fig 4

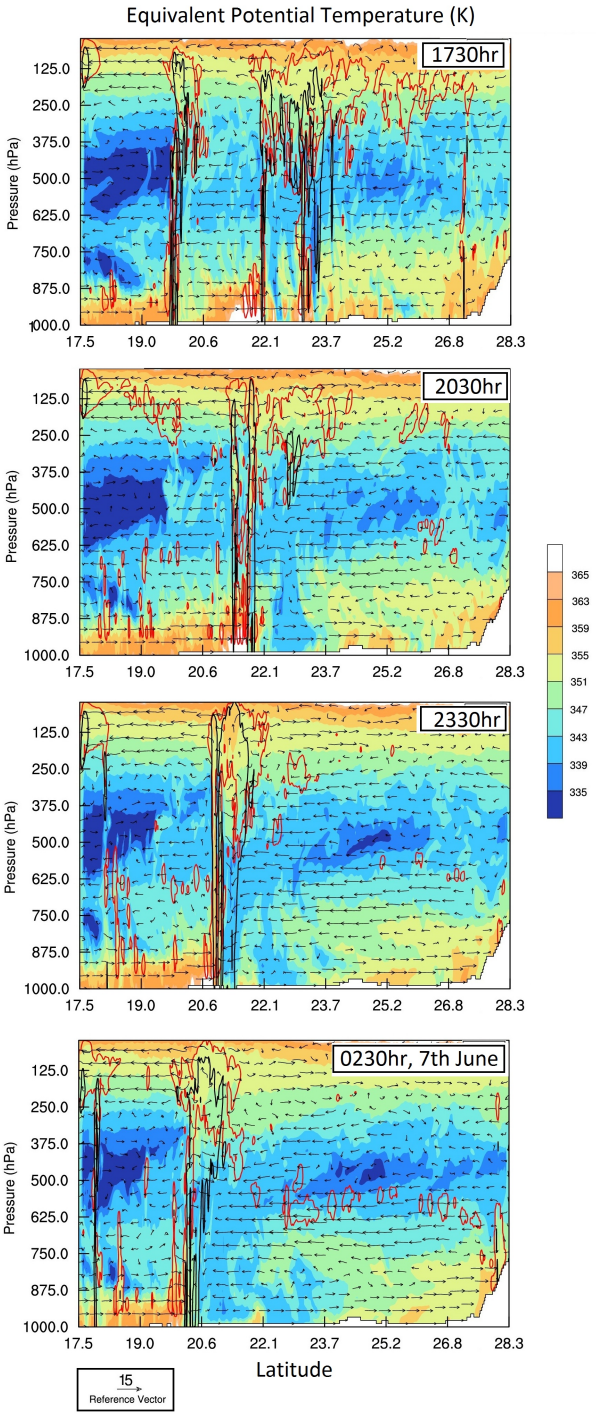

Figure 9. Similar to Fig 8 showing intensification of convection and the mature stage of convection (local time on top right corner).

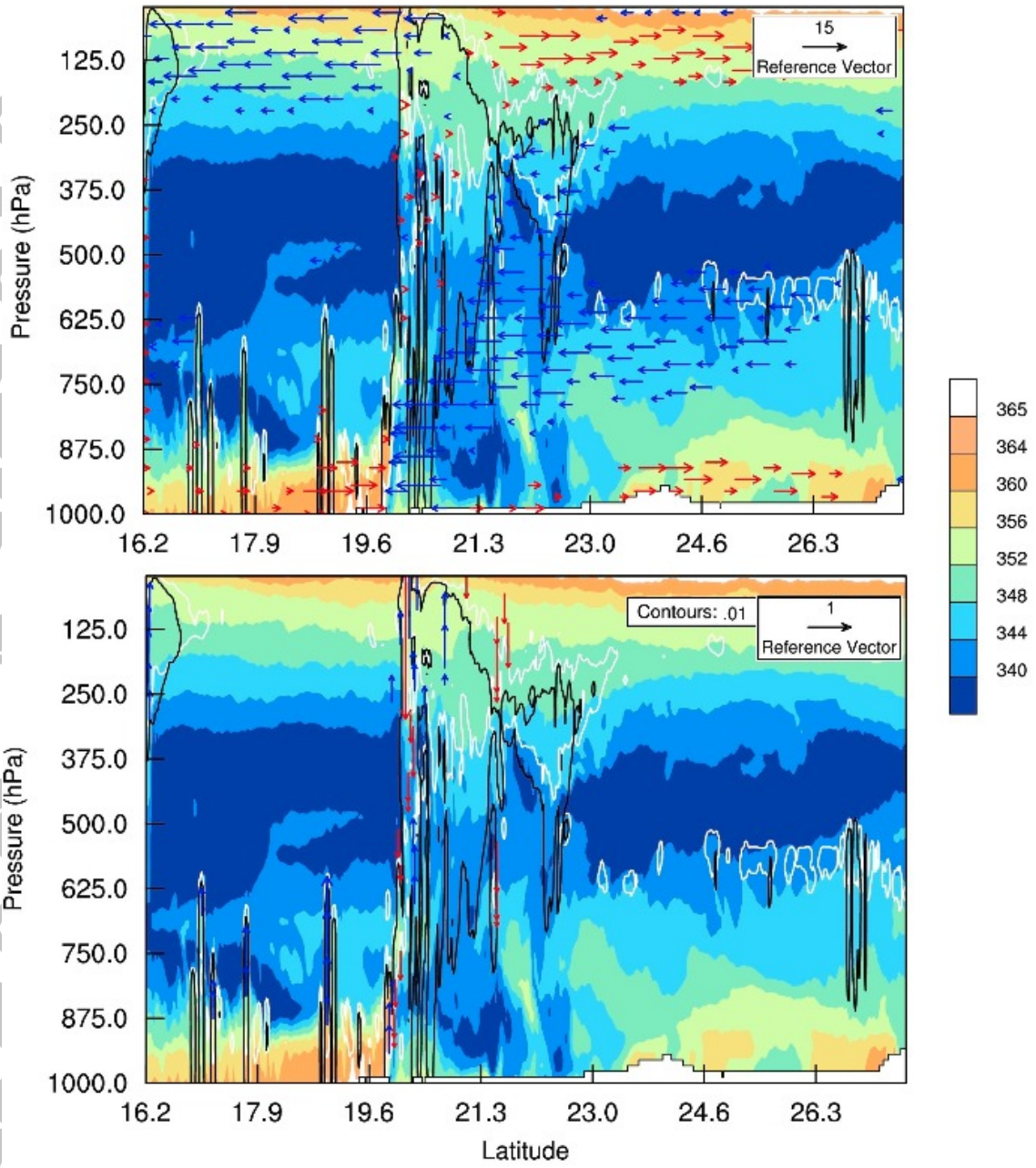

Figure 10. Similar to Fig 8 showing cross-section plot with equivalent potential temperature (colored), cloud water mixing ratio (black contour), rain water mixing ratio (white contour) with separate meridional (top panel, greater than 5 m/s) and vertical (bottom panel, greater than 1 m/s) winds vectors along the cross-section for an event at 2330 hour 6 June, 2008.

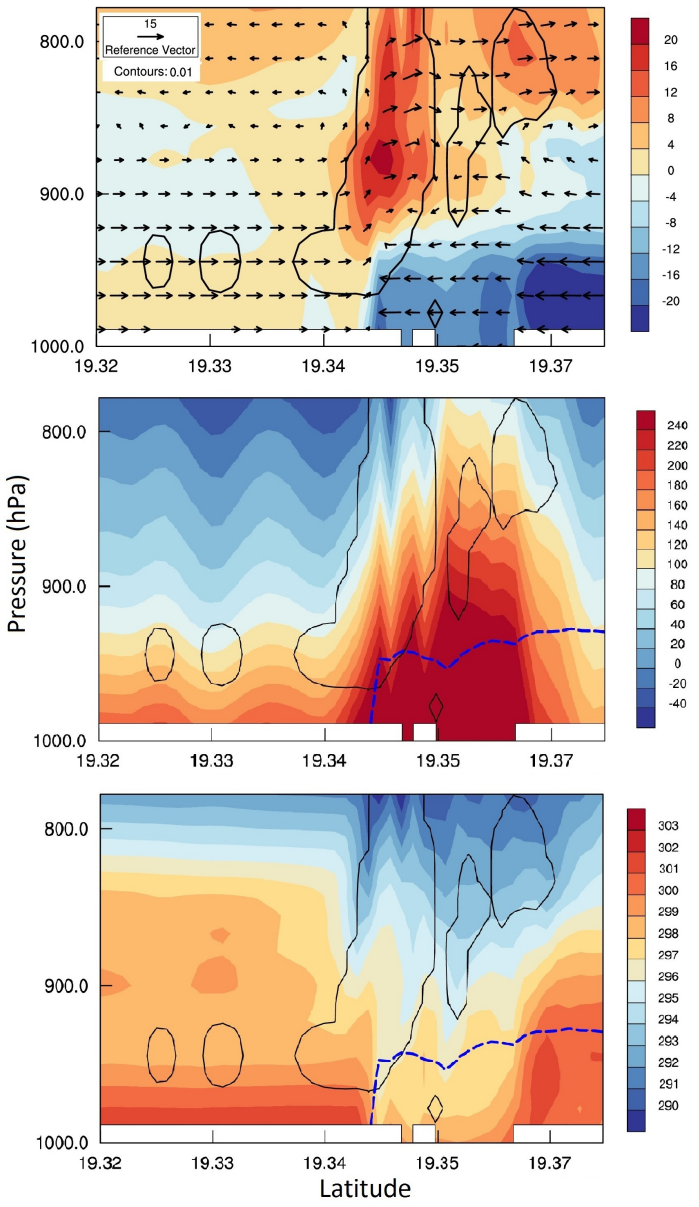

Figure 11. Top panel - Anomaly of equivalent potential temperature when the system is present (2330 local time, 6 June) and actual winds (no anomaly) in the region from when there is no system 6 hours back. The contour (0.01g/kg) shows cloud water mixing ratio. The thick line arrows show general direction of motion for the air parcels. Middle panel shows perturbation pressure for the MCS. The thick-dashed contour line shows negative equivalent temperature. The lowest panel shows actual air temperature of the system.

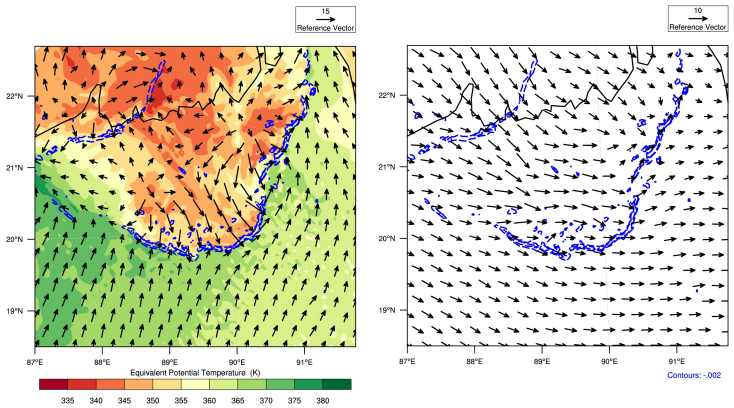

Figure 12. Left panel shows convergence at the leading edge of MCS at 975 hPa (blue contour line), the colormap shows equivalent potential temperature averaged over 990 to 960 hPa, and vectors are averaged over 990 to 960 hPa. Right panel shows convergence at the leading edge of MCS at 975 hPa and velocity vector averaged over cloud layer (900 to 350 hPa). Low-level jet refers to the winds south of convergence zone in the left panel where the equivalent potential temperature is generally greater than 360K. This is the region which is ahead of the southward propagating MCS. The rear inflow jet or the cold pool velocity refers to the wind vectors in the left panel just north of convergence zone (here the equivalent potential temperature is generally less than 350K). The wind vectors in the right panel refers to the advective component of the MCS.

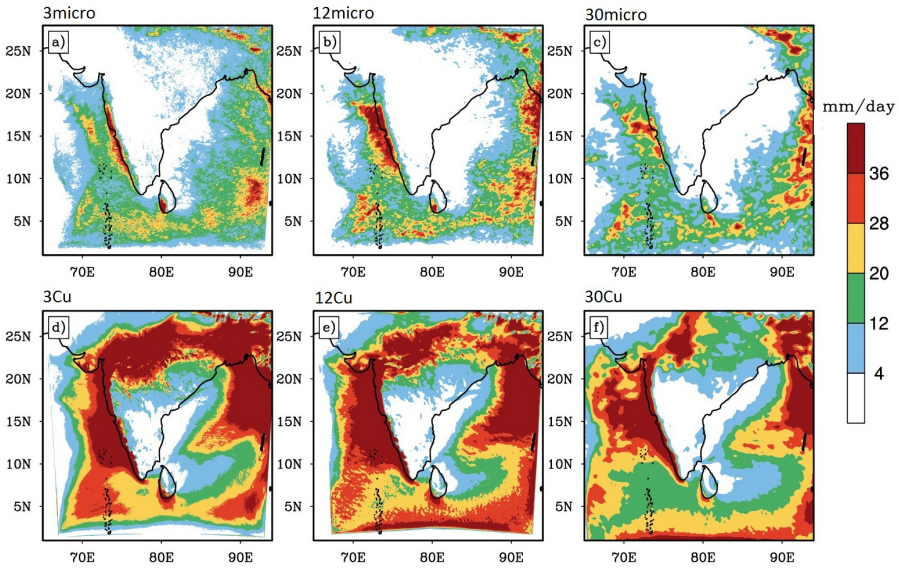

Figure 13. Monthly mean (June) model precipitation at 3, 12, 30 km horizontal resolutions and with explicit microphysics and cumulus parameterization. The details of the simulations are mentioned in Table 1.

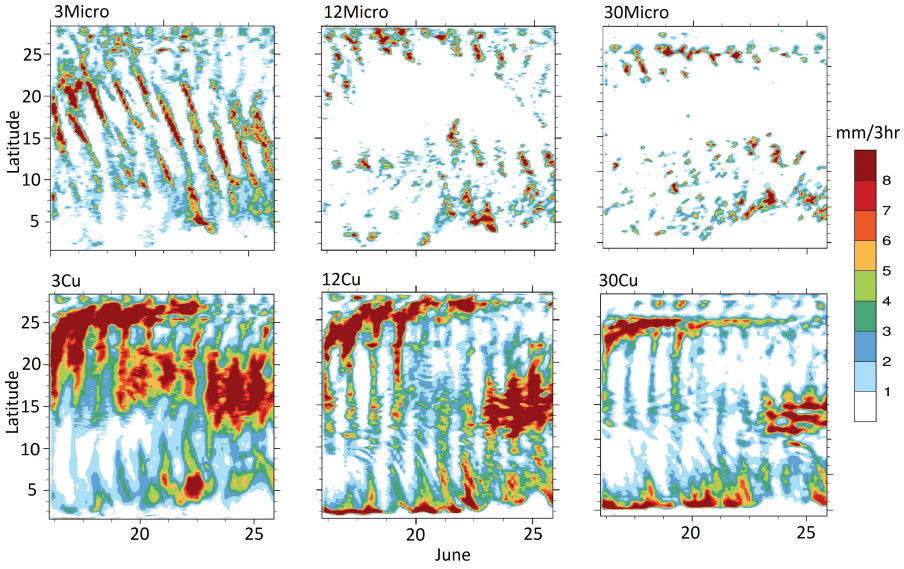

Figure 14. Meridional Propagation of precipitation averaged over 85-90°E with different model resolution and convection representation shown in Table 1.

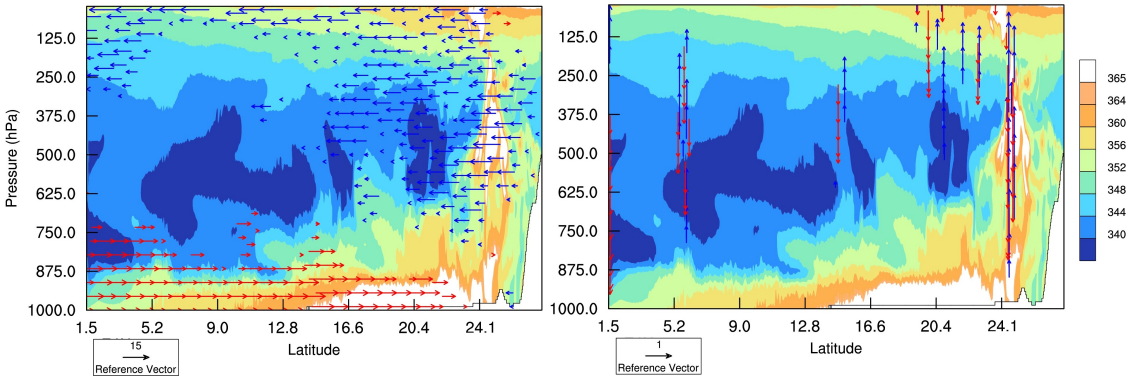

Figure 15. Cross section plot for 3Cu case showing equivalent potential temperature vertical structure for a raining system near 24°N. Left panel shows meridional winds greater than 5 m/s, while vertical winds greater than 1 m/s are shown in the right panel.

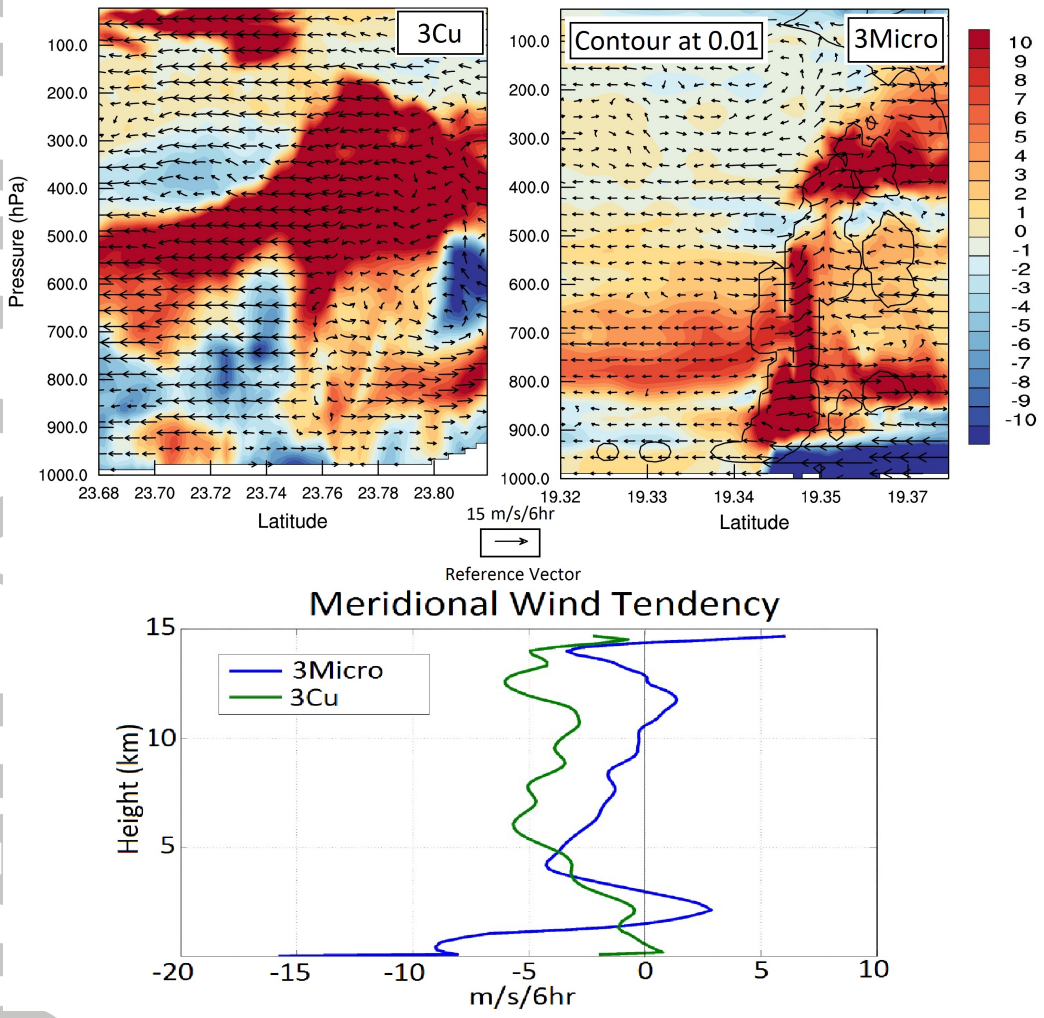

Figure 16. Vertical cross-section plot for for cumulus convection (3Cu) and explicit microphysics schemes (3Micro) case showing heating tendency due cumulus convection and explicit microphysics. The shaded region is the equivalent potential temperature anomaly and the contour shows cloud water mixing ratio of the present system (in microphysics case only). Lower panel shows horizontal mean of tendencies over the top 2 panels

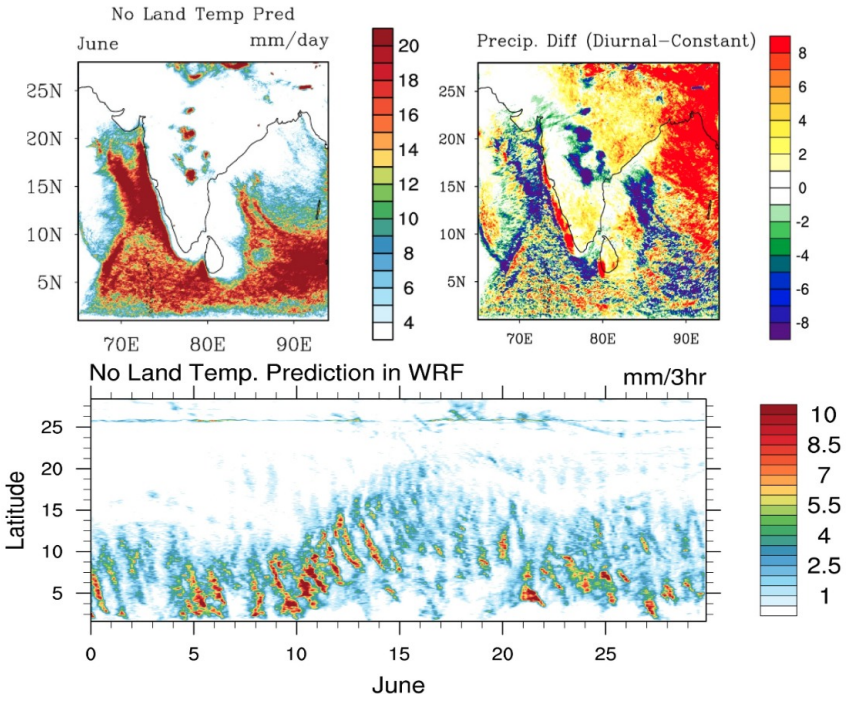

Figure 17. Precipitation produced by model with constant land surface temperature (top left), difference in precipitation of constant land surface temperature simulation from diurnal land surface temperature(top right), and southward propagations over BoB with constant land temperature